CHALMERS
UNIVERSITY OF TECHNOLOGY

Impact Of The Locations Of The Control Points On Optimal Solutions For Self-Bending Beamforming

BeBeC-2018-D21

IMPACT OF THE LOCATIONS OF THE CONTROL POINTS ON OPTIMAL SOLUTIONS FOR SELF-BENDING BEAMFORMING

Jens Ahrens
Division of Applied Acoustics
Chalmers University of Technology
412 96 Gothenburg, Sweden
jens.ahrens@chalmers.se

Abstract

Self-bending beamformers exhibit a sensitivity that bends over space in the nearfield of the array. They were derived from caustic wave fields and have been presented in the literature recently. It is fairly straightforward to obtain an analytic solution for the phase profile that has to be imposed onto the array elements. This approach is termed phase engineering. Deriving the corresponding gain profile is less straightforward. Solutions that have been proposed in the literature so far are educated guesses as well as numerically optimal solutions. The latter are the topic of the presented work. We use a convex approach. We show that the locations of both the (single) target control point in the bright zone as well as the (many) control points in the dark zone have a significant impact on the resulting beam. Particularly, the control point locations in the dark zone have to be chosen carefully so that the desired dark zone actually evolves. Choosing the target control point close to the caustic creates the largest beam gradient along the caustic. A remarkable observation is that prescribing a phase profile onto the elements of the array can also have a detrimental effect, and solving for the complex beamformer weights can yield a better result. Based on the observations we conclude that minimizing the norm of the beamformer weights does not seem to be the most favorable approach for the present problem.

1 Introduction

Self-bending wave fields were first predicted in the field of quantum mechanics [5] and made their way to acoustics via optics [14]. In optics, a phase profile is imposed onto a beam of light via a phase mask, for example a transparent material of appropriately varying thickness [9]. The phase profile that is imposed is taken from an optical wave front that forms a caustic. A caustic occurs if the family of rays that represent the wave front exhibit an envelope and are tangent to

that envelope. This envelope is then referred to as caustic. The same concept was applied to acoustic fields in [17, 18] using an array of acoustic transducers that controlled the phase profile of the evolving sound field.

The literature mentioned above focuses on the creation of self-bending wave fields. The application of the concept to sensor arrays to achieve a self-bending sensitivity was proposed in [2], which opens a new line of conceivable practical implementations. The mechanisms for creating self-bending waves and self-bending sensitivities are essentially identical due to the reciprocity of the Helmholtz equation. We will simply speak of self-bending beams in the remainder of this paper, which may refer to either case.

The resulting beams exhibit distance dependent properties. A closely related domain is nearfield beamforming, where a distance-dependent beam is typically achieved by taking the curvature differences between planar and spherical waves into account [8, 11, 12, 19]. Both the gain and the delay (or, equivalently, the complex weights) are determined for each of the array elements. The extent to which physical limitations are taken into account in nearfield beamforming is typically limited so that robustness is achieved by regularization, which comes at the price of a reduction in the performance that is difficult to control.

While deriving the phase profile that needs to be imposed on the element of an array is straightforward, the original solution for self-bending beamforming employed educated guesses for the gain profile [2]. A numerical solution for based on convex optimization was proposed in [3]. For the investigated simple scenario, the performance of the optimal beamformer was similar to the analytically derived one (i.e., the guessed solution). It was pointed out that it depends fundamentally on the choice of location of the control points inside the dark zone how well the self-bending property forms.

In the present paper, we summarize the basics of caustics and self-bending beamforming and investigate a selected set of scenarios to shed more light on the dependency of the self-bending property on the location of the control points based on a set of scenarios.

2 Self-Bending Wave Fronts

Self-bending wave fields are essentially fields that are composed of wave fronts that fold along a caustic. As the Airy integral developed in the 1930s by Sir George Biddell Airy is a powerful tool for explaining caustics, such waves are termed *Airy wavepackets* or *Airy beams* in electromagnetics and in optics.

Obviously, the wave itself is not accelerated. Rather, the amplitude envelope of the wave field appears to be bent. The concept of [17, 18] is illustrated in Fig. 1(a): A caustic is pre-defined along which the wave front folds. In the high-frequency limit, the wave front does not traverse the caustic. It is important to note that self-bending waves evolve only in the high-frequency limit. This high-frequency limit is fulfilled if the considered wavelength is much smaller than the curvature of the caustic. More generally, any significant changes to the wave amplitude have to evolve at length scales much larger than the wavelength. Note that the caustic needs to be convex in order that the wave perfectly avoids a given region in the high-frequency limit.

We choose the sample caustic from [2, 17], which is given by the cubic Bézier curve

$$B(t) = (1-t)^3 B_0 + 3t(1-t)^2 B_1 + 3(1-t)t^2 B_2 + t^3 B_3 \,, \tag{1}$$

with

$$B_0 = [0, -0.2311]^T, \qquad B_1 = [0.1, 0.0189]^T$$
$$B_2 = [0.25, 0.1689]^T, \qquad B_3 = [0.98, -0.3311]^T ,$$

to allow for a direct comparison of the results. We limit our observations to the x-y-plane so that we define the four points that define the Bézier curve as $B_i = [x_i, y_i, 0]^T$. The red line in Fig. 1(a) illustrates (1). Note that the control variable t does not represent the traveled distance along $B(t)$, nor is it directly proportional to time when a wave moves along $B(t)$.

3 Creation of Self-Bending Waves

As proven by, for example, Rayleigh's first integral formula, a wave field can be synthesized if its directional gradient is known along a reference plane and if there is a continuous distribution secondary monopole sources along this reference plane [16]:

$$P(\mathbf{x}, \omega) = \iint_{-\infty}^{\infty} \underbrace{2 \frac{\partial}{\partial \mathbf{n}} S(\mathbf{x}, \omega)\big|_{\mathbf{x}=\mathbf{x}_0}}_{=D(\mathbf{x}_0, \omega)} G(\mathbf{x}_0, \mathbf{x}, \omega) d\Omega(\mathbf{x}_0) \, . \tag{2}$$

$P(\cdot)$ denotes the harmonic scalar wave field that evolves due to the monopole distribution along the reference plane. $G(\mathbf{x}, \mathbf{x}_0, \omega) = \frac{1}{4\pi} \frac{e^{-\mathrm{i}\omega/c|\mathbf{x}-\mathbf{x}_0|}}{|\mathbf{x}-\mathbf{x}_0|}$ is the free-field Green's function, i.e. the spatio-

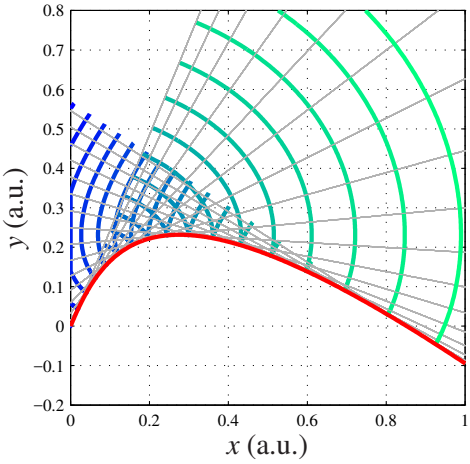

(a) Schematic of the principle of self-bending wave fronts via rays; the red line indicates the prescribed caustic given by (1); the gray lines are sample tangents of the caustic; the blue/green lines are sample wave fronts; time may evolve from blue to green as well as from green to blue

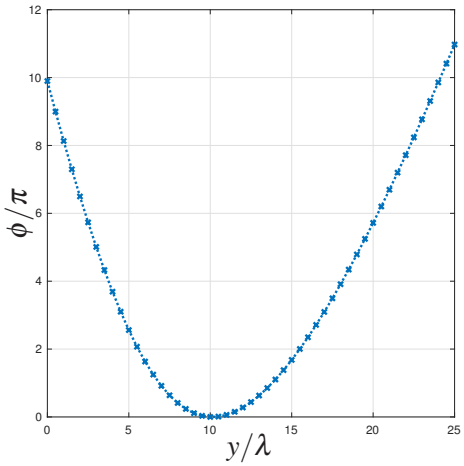

(b) Unwrapped phase profile $\phi(\cdot)$ of the arrays depicted in Fig. 2

Figure 1: Schematic of a caustic and corresponding phase profile at the reference line $x = 0$

temporal transfer function of the secondary monopole sources. $S(\cdot)$ is an arbitrary virtual scalar wave field that is source-free in the target half-space that is bounded by the reference plane. $d\Omega(\cdot)$ is an infinitesimal surface element. $\mathbf{x}_0$ is a position on the reference plane.

When the secondary monopoles are driven with two times the gradient $\partial/\partial\mathbf{n}$ of $S(\cdot)$ in direction normal to the boundary and evaluated at the boundary, then the synthesized wave field $P(\cdot)$ is identical to the virtual (prescribed) field $S(\cdot)$ inside the target half-space. It is proven in the Appendix that the phase profile $\angle D(\cdot)$ of the driving signal is identical to the phase $\phi(\mathbf{x}_0, \omega)$ of the harmonic field at the positions of the secondary sources. It is therefore possible to create a self-bending wave by imposing the back traced phase profile of the self-bending wave onto a planar array of sufficiently densely spaced transducers. This approach is termed *phase engineering* [17, 18].

Eq. (9) in the Appendix also shows that the purely real gain (or *amplitude profile*) $|D(\cdot)|$ of the secondary sources is given by $A(\mathbf{x}_0, \omega)\phi'(\mathbf{x}_0, \omega)$, whereby $A(\cdot)$ is the amplitude distribution of the self-bending field along the reference plane, The prime $'$ represents spatial differentiation.

4 Linear Arrays

Planar transducer arrays are inconvenient as the required number of elements is high. When wave field synthesis inside a given plane is targeted, then also linear arrays may be employed. The driving functions $D(\cdot)$ are identical to those for planar arrays apart from a global frequency dependent factor. This type of scenario is termed 2.5-dimensional and is well known in sound field synthesis [1]. The curvatures of the wave fronts that evolve are identical to the prescribed ones inside the target half-plane. The control over the amplitude decay of the synthesized field over distance to the array is limited. The synthesized wave field is obviously invariant with respect to rotation about the axis through the array's elements.

For convenience, we assume a linear array of transducers here. Due to the reciprocity of the Helmholtz equation, we may interpret the beam as the amplitude distribution of the synthesized sound field (when loudspeakers are assumed) or as amplitude distribution of the array's sensitivity (when microphones are assumed).

5 Optimal Array Pattern Synthesis

A vast amount of literature exists on numerically optimal array pattern synthesis in the domain of beamforming both for signal-dependent scenarios as well as for the present case of signal-independent scenarios [15]. A variety of optimality criteria exist. A typical criterion for signal-independent farfield scenarios is maximizing the so-called white noise gain (WNG) [10], which represents the gain of the target signal (i.e., the desired signal) that the beamformer achieves relative to spatially white noise. A convex solution incorporating a constraint on the WNG of a farfield beamformer is presented in [13]. This scheme is not convenient in the present case as it is inconvenient to define what is the location of the target signal as there are many useful options.

We therefore adapt the approach that is typically applied in nearfield beamforming: We assume a discrete set of array elements and find the set of weights $D(\mathbf{x}_0, \omega)$ that minimize the beam amplitude in the dark zone (signals from which are intended to be suppressed) while maintaining unit amplitude at the target location [12]. This can lead to very aggressive and therefore

non-robust solutions, which are not applicable when the actual array exhibits the slightest deviations from the assumptions. A lack of robustness is typically an indication for a large range of gains of the array elements. Regularization can be applied, which modifies the solution in order to squash this range at the expense of an (uncontrolled) reduction in performance.

We employ the convex approach from [7] here in which we specify the performance and aim at finding the set of gains with the lowest norm $\|D(\cdot)\|$ that enables the desired performance. $D(\cdot)$ is the vector containing the weights of all (discrete) array elements. Searching for the lowest norm inherently squashes the range of weights with relaxation of the performance requirements.

More explicitly, the present optimization problem reads

$$\min\|D(\mathbf{x}_0,\omega)\| \tag{3}$$

subject to

$$\mathbf{G}(\mathbf{x}_0,\mathbf{x}_t,\omega)D(\mathbf{x}_0,\omega) = 1, \tag{3a}$$

$$|\mathbf{G}(\mathbf{x}_0,\mathbf{x}_d,\omega)D(\mathbf{x}_0,\omega)| \leq 10^{\frac{C}{20}} \tag{3b}$$

whereby C denotes the desired attenuation in dB at the control points $\mathbf{x}_d$ in the dark zone relative to the target location control point $\mathbf{x}_t$ in the bright zone.

$$\mathbf{G}(\mathbf{x}_0,\mathbf{x}_t,\omega) = \begin{bmatrix} e^{-\mathrm{i}\phi_1(\omega)}G(\mathbf{x}_{0,1},\mathbf{x}_t,\omega) \\ e^{-\mathrm{i}\phi_2(\omega)}G(\mathbf{x}_{0,2},\mathbf{x}_t,\omega) \\ \vdots \\ e^{-\mathrm{i}\phi_N(\omega)}G(\mathbf{x}_{0,N},\mathbf{x}_t,\omega) \end{bmatrix}^T \tag{4}$$

is a vector containing the transfer paths from the N individual array elements indexed by n to the target location in the bright zone, and

$$\mathbf{G}(\mathbf{x}_0,\mathbf{x}_d,\omega) = \begin{bmatrix} e^{-\mathrm{i}\phi_1(\omega)}G(\mathbf{x}_{0,1},\mathbf{x}_{d,1},\omega) & \dots & e^{-\mathrm{i}\phi_N(\omega)}G(\mathbf{x}_{0,N},\mathbf{x}_{d,1},\omega) \\ e^{-\mathrm{i}\phi_1(\omega)}G(\mathbf{x}_{0,1},\mathbf{x}_{d,2},\omega) & \dots & e^{-\mathrm{i}\phi_N(\omega)}G(\mathbf{x}_{0,N},\mathbf{x}_{d,2},\omega) \\ \vdots & \vdots & \vdots \\ e^{-\mathrm{i}\phi_1(\omega)}G(\mathbf{x}_{0,1},\mathbf{x}_{d,M},\omega) & \dots & e^{-\mathrm{i}\phi_N(\omega)}G(\mathbf{x}_{0,N},\mathbf{x}_{d,M},\omega) \end{bmatrix} \tag{5}$$

is a matrix containing the transfer paths from the N individual array elements to the M control points in the dark zone. Note that we search for purely real $D(\cdot)$. The phase engineering is performed by incorporating the caustics-based phase profile $\phi(\mathbf{x}_0,\omega)$ into the transfer paths $\mathbf{G}(\mathbf{x}_0,\mathbf{x}_d,\omega)$.

6 Results

Refer to Fig. 2 for sample monochromatic self-bending beams based on the caustic that is defined by (1) and depicted in Fig. 1(a). The array of isotropic (monopole) elements extends along the y-axis from $y = 0$ to $y = 25\lambda$. Fig. 1(b) depicts the phase profile that was imposed

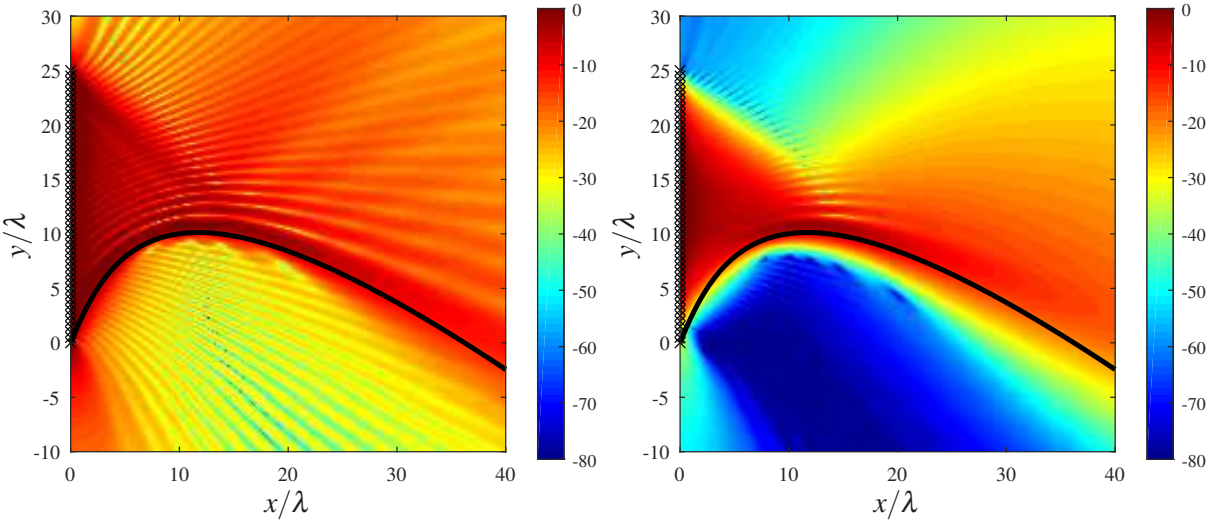

(a) Equal amplitude of 1 imposed on all array elements (b) Cosine-squared amplitude profile imposed on the array elements

Figure 2: Magnitude in dB of the beam of a sample linear array of 51 isotropic (omnidirectional) elements of length $L = 25\lambda$ located on the y-axis; the element spacing is $\Delta y = 0.5\lambda$ (i.e. critically spaced); the black marks indicate the locations of the array elements; the black line represents the caustic

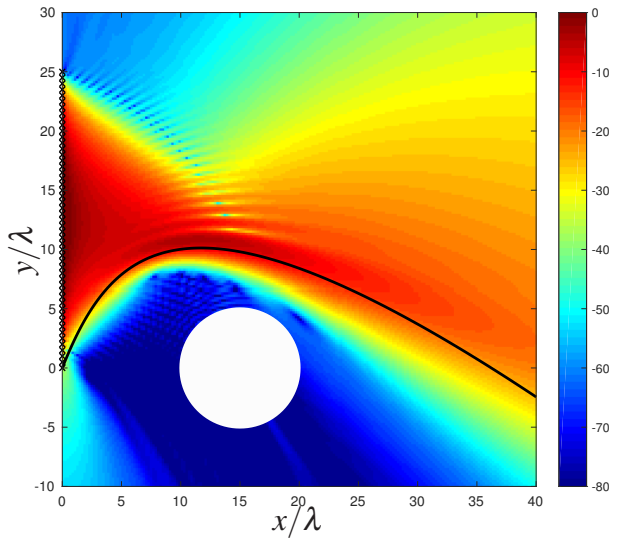

Figure 3: Sensitivity of the array from Fig. 2(b) in the presence of a rigid spherical scattering object (indicated by the white disc)

on the array elements. Fig. 2(a) shows the resulting beam amplitude when an equal purely real gain is imposed on the array elements additionally to the phase profile. This corresponds to the approaches presented in [17, 18]. The attenuation in the quiet zone is in the order of 20 dB compared to locations along the caustic. Fig. 2(b) shows the resulting beam when a

cosine-squared shaped weighting is imposed on the array elements. The difference to Fig. 2(a) is eminent [2]. A pronounced quiet zone evolves south of the caustic indicated by the black line. The attenuation in the quiet zone is in the order of 60 dB or more compared to locations along the caustic. Note that the cosine-squared shaped amplitude profile works well in the present scenario. It cannot be considered a general solution.

A noteworthy property of the beamformer is that it rejects all sound that originates from the dark zone directly or indirectly. This means that it also rejects all signals that are reflected by objects located in the dark zone. This circumstance is illustrated in Fig. 3, which shows the beamformer from Fig. 2(b) but with a rigid spherical object present in the dark zone. Note that the presence of this object does not influence beamformer's sensitivity.

Fig. 4 depicts the numerical solutions for the scenario from Fig. 2(b) according to (3).

A remarkable observation is that although we are solving (3) for purely real weights in Fig. 4(a)-(c), it is generally not such that all weights exhibit the same algebraic sign like our physical model of phase and magnitude would suggest it. (Note that a change in sign is equivalent to a phase jump by π.)

Another important observation when comparing Fig. 4(a)-(c) is that the choice of control points has a fundamental effect on the spatial evolution of the beam [3]. The mere prescription of a phase profile onto the array elements does not narrow down the solution space sufficiently. However, it seems unreasonable to sample the dark zone densely with control points. The contour in Fig. 4(c) is a shifted copy of a segment of the prescribed caustic and constitutes a useful choice. It prevents the beam from entering the dark zone.

Instead of solving (3) for purely real weights, we can, of course, also skip prescribing a phase profile and solve for complex weights. At first sight, we are thereby removing all physics from the problem. However, by using the same control points like in Fig. 4(b), we are inherently assuming the solution to be related to the modelled caustic. The result depicted in Fig. 4(d) is very comparable to Fig. 4(c). Bear in mind that we have two times the amount of variables to solve for (the real part as well as the imaginary part of the weights) so that it appears useful to choose two times as many control points. Remarkably, the resulting phase profile is very similar to the manually derived one apart from a constant offset (see the top-left inset in Fig. 4(d)).

Fig. 5 depicts variations of the scenario from Fig. 4(c). Fig. 5(a) uses a control point spacing $\Delta\mathbf{x}_d$ that is precisely 0.5λ, whereas Fig. 5(b) uses exactly the same contour of control points but only half the amount and with $\Delta\mathbf{x}_d = \lambda$. Note that the problem is significantly underdetermined in the latter case. Still, the problem is solved, i.e., the optimization conditions (3a) and (3b) are fulfilled, and the resulting beam pattern is useful. Keeping $\Delta\mathbf{x}_d = \lambda$ but using a sufficient number control points to have an overdetermined solution as in Fig. 5(a) increases the attenuation in the dark zone. This suggests that the control point spacing $\Delta\mathbf{x}_d$ is not the only decisive factor.

The underdetermined solution with narrow control point spacing in Fig. 5(c) is also viable (the optimization conditions (3a) and (3b) are fulfilled), but the resulting dark zone is smaller than desired.

Fig. 6 and 7 depict a self-bending beamformer based on a caustic given by the polynomial

$$y = -0.01 * (x+2)^3 - 0.06 * (x+2)^2 + 0.32\,, \tag{6}$$

and Fig. 8 depicts a self-bending beamformer based on the polynomial from (6) but rotated by 30°. This yields a curvature of the caustic that is significantly more gentle than the one from the previous figures.

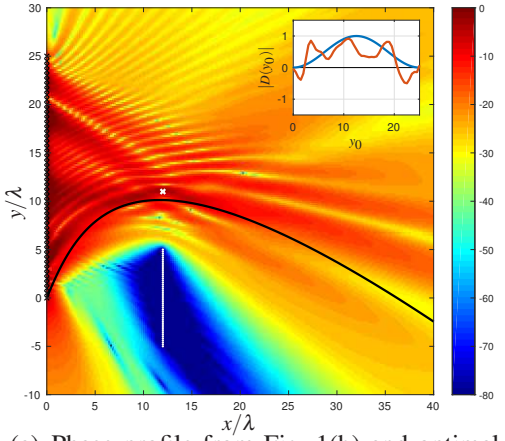

(a) Phase profile from Fig. 1(b) and optimal real weights; 52 control points were used (51 + 1)

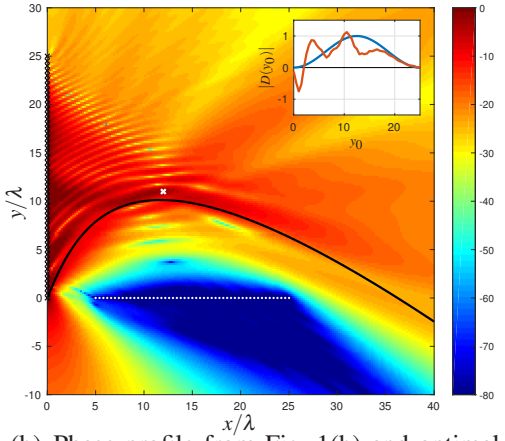

(b) Phase profile from Fig. 1(b) and optimal real weights; 52 control points were used (51 + 1)

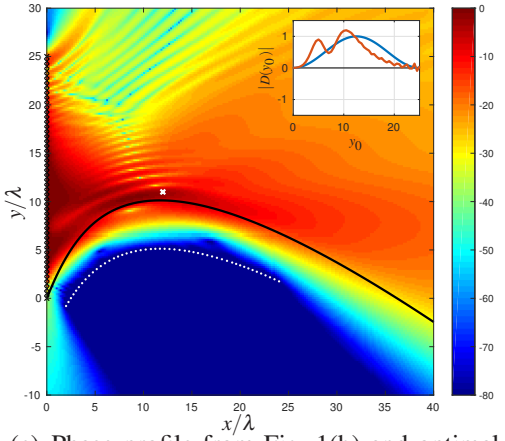

(c) Phase profile from Fig. 1(b) and optimal real weights; 52 control points were used (51 + 1)

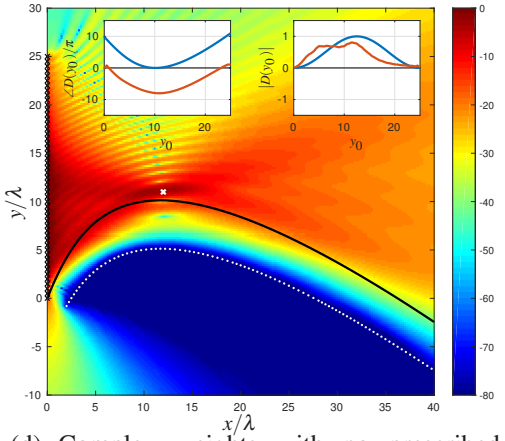

(d) Complex weights with no prescribed phase profile; 93 control points were used (92 + 1); the top-left inset shows the resulting phase contour with the analytically derived profile from Fig. 1(b) as reference

Figure 4: Magnitude in dB of the beams produced by the array from Fig. 2 using optimal solutions according to (3)*; $C = -80$ dB; the white cross marks the control point in the bright zone; the white points mark the control points in the dark zone; the top-right inset shows the resulting real gain profile (orange) with the cosine-square profile as reference (blue)*

Using the phase profile determined by the caustic as well as a cosine-squared amplitude profile yields a useful beam pattern as depicted in Fig. 6(a). For investigating the optimal solutions, we always use the same 205 control points in the dark zone but vary the location of the target control point in the bright zone. Fig. 6(b)-(d) depict the result of the optimization for complex weights $D(\cdot)$. It can be seen that the a dark zone arises in the desired manner. The structure of the beam in the bright zone varies significantly with the location of the target control point $\mathbf{x}_t$. Choosing $\mathbf{x}_t$ close to the caustic causes the strongest gradient of the beam along the

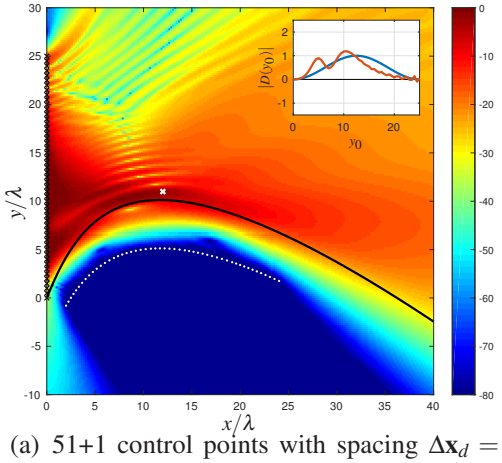

(a) 51+1 control points with spacing $\Delta\mathbf{x}_d = 0.5\lambda$

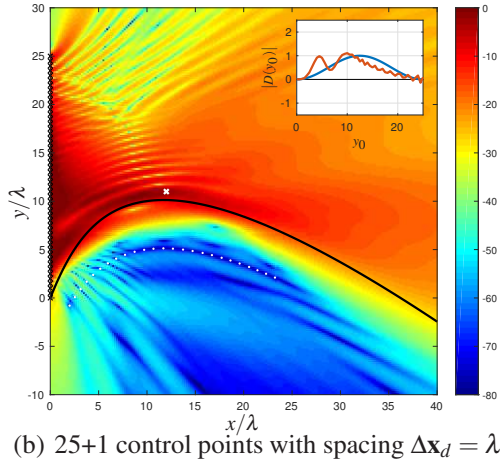

(b) 25+1 control points with spacing $\Delta\mathbf{x}_d = \lambda$

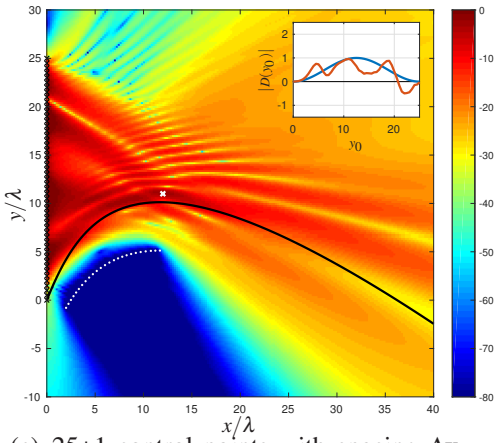

(c) 25+1 control points with spacing $\Delta\mathbf{x}_d = 0.5\lambda$

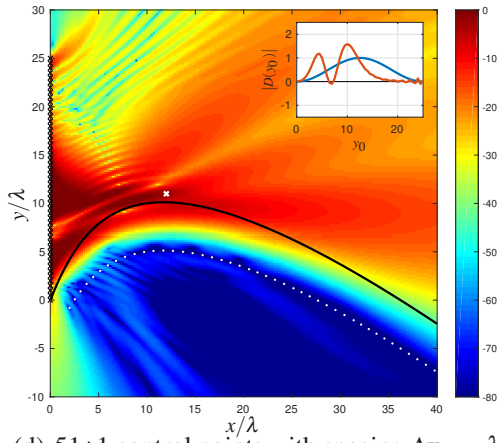

(d) 51+1 control points with spacing $\Delta\mathbf{x}_d = \lambda$

Figure 5: Variations over the scenario from Fig. 4(c)

caustic. The resulting phase profile can depart considerably from the one derived based on the prescribed caustic (see the bottom insets).

Fig. 7 depicts the same scenario but with the phase profile prescribed and optimized for purely real weights. Remarkably, the resulting beam departs significantly from the desired one. It is even such that the optimization problem is not solved in Fig. 7(b) and (c). This is despite the fact that the prescription of the caustic's phase profile adds meaningful physical contraints to the problem.

Finally, Fig. 8 uses the caustic described by (6) and rotated by 30°. The observations are equivalent to the ones made with Fig. 6 and 7, i.e., a dark zone forms as desired, the structure of the beam in the bright zone depends strongly on the location of the target control point in the bright zone, and imposing the manually derived phase profile can lead to unusable results. We only present the simulations of the optimization for the complex weights for convenience.

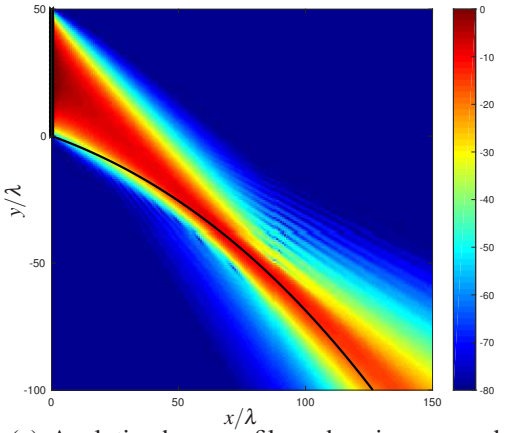

(a) Analytic phase profile and cosine-squared amplitude profile

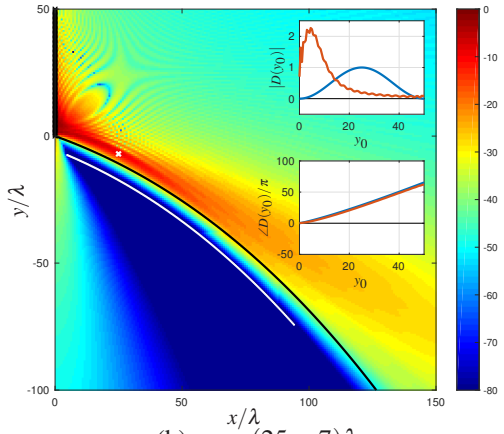

(b) $\mathbf{x}_t = (25, -7)\lambda$

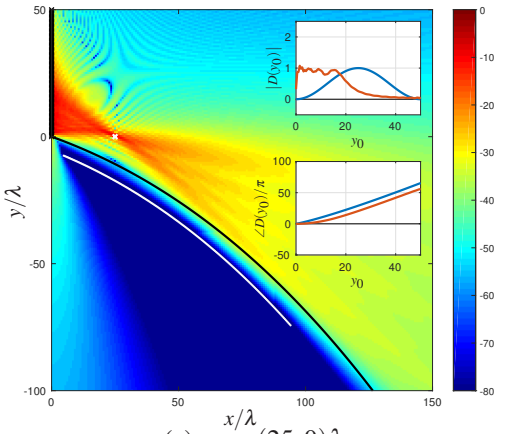

(c) $\mathbf{x}_t = (25, 0)\lambda$

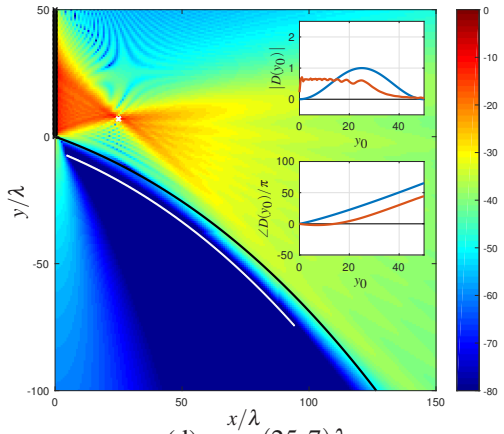

(d) $\mathbf{x}_t = (25, 7)\lambda$

Figure 6: Magnitude in dB of the beams produced by a critically-spaced array of length $L = 50\lambda$ using optimal solutions according to (3) *for different locations of the control point $\mathbf{x}_t$ in the bright zone; $C = -80$ dB; the caustic is given by* (6)*; the white cross marks $\mathbf{x}_t$; the white points mark the 205 control points in the dark zone; the optimization was performed for the complex weights $D(\mathbf{x}, \omega)$; no phase profile was imposed*

7 Conclusions

We investigated the impact of the control point locations on optimal solutions for self-bending beamforming. We showed that the choice of control points in the dark zone has to be made with care so that the dark zone actually evolves as desired. There is somewhat more freedom in choosing the target control point in the bright zone, which can have a considerable impact on the structure of the beam in the bright zone.

The problem may be underdetermined and still solvable. Choosing so few control points that an underdetermined problem evolves seems to have an unfavorable effect on the attenuation in the dark zone. Similarly, the spacing between the control points in the dark zone may be larger than half a wavelength. The loss in attenuation is only moderate in this case.

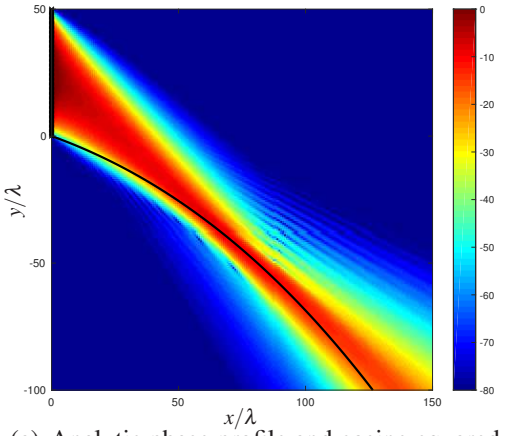

(a) Analytic phase profile and cosine-squared amplitude profile imposed

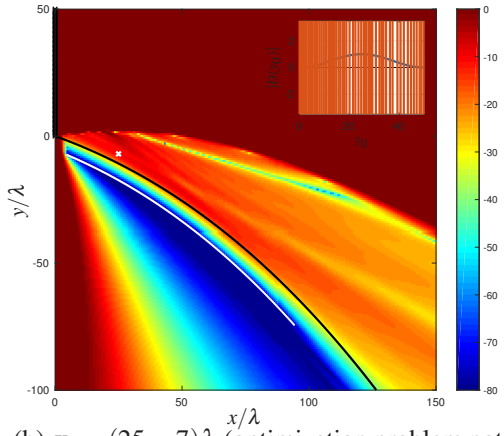

(b) $\mathbf{x}_t = (25, -7)\lambda$ (optimization problem not solved)

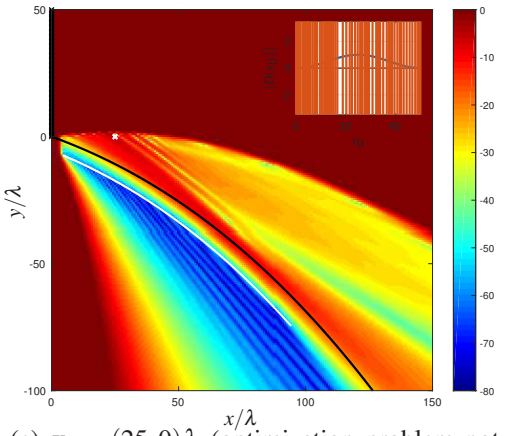

(c) $\mathbf{x}_t = (25, 0)\lambda$ (optimization problem not solved)

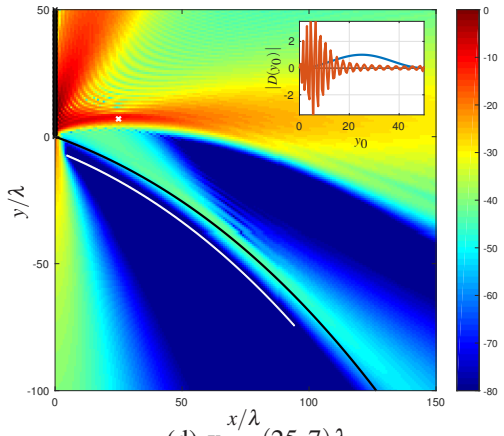

(d) $\mathbf{x}_t = (25, 7)\lambda$

Figure 7: Same scenario like in Fig. 6 but with the manually derived phase profile imposed (and optimized of the purely real gains)

Certain types of self-bending beams do not benefit from prescribing a phase profile, which was manually derived from the caustic underlying the self-bending wave field. Quite in contrary, we have achieved as good or sometimes even much better solutions when optimizing for the complex beamformer weights without prescribing any phase profile and therefore no explicit consideration of the desired caustic. This caustic is still implicitly considered due to the choice of the locations of the control points. This suggests that minimising the norm of the beamformer weights is not the most ideal approach for the present problem. A more physics-inspired solution is desired.

The investigation of the robustness of the approach was beyond the scope of this paper. The reader is referred to the results from [2] obtained that were obtained with a cosine-squared window.

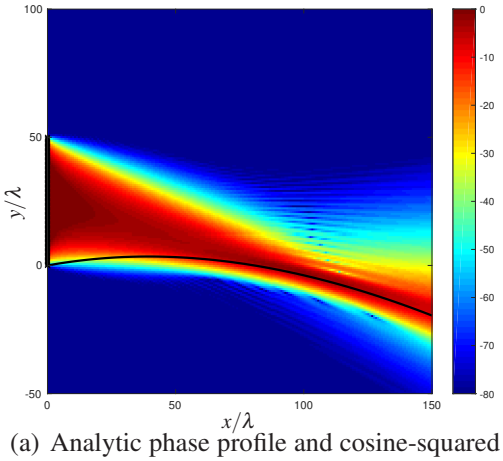

(a) Analytic phase profile and cosine-squared amplitude profile

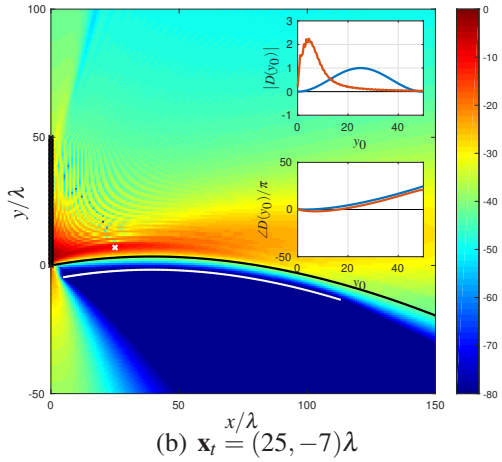

(b) $\mathbf{x}_t = (25, -7)\lambda$

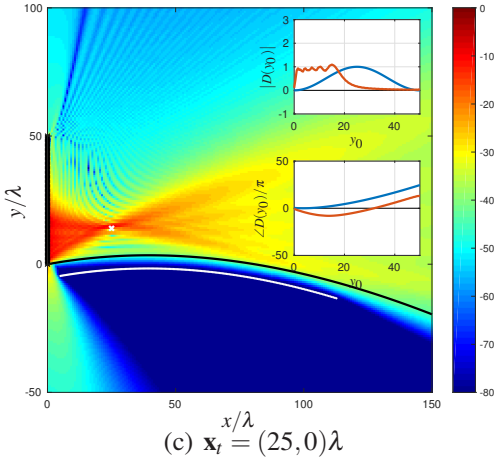

(c) $\mathbf{x}_t = (25, 0)\lambda$

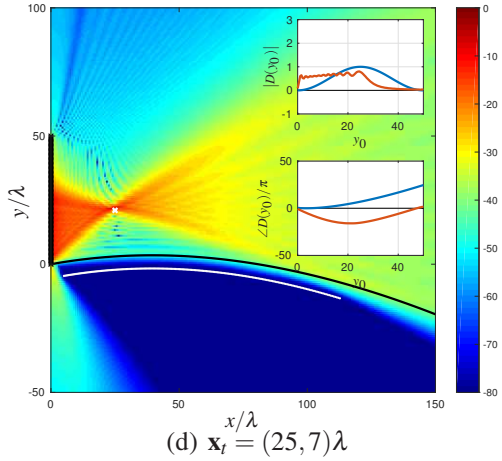

(d) $\mathbf{x}_t = (25, 7)\lambda$

Figure 8: Same situation like in Fig. 6 but with the caustic rotated by 30°

APPENDIX: DERIVATION OF THE SECONDARY SOURCE PHASE PROFILE

Consider the driving function $D(\mathbf{x}_0, \omega)$ for the secondary source at $\mathbf{x}_0$ to synthesize a sound pressure field $S(\mathbf{x}, \omega)$ as given by (2). The directional gradient $\frac{\partial}{\partial \mathbf{n}}$ is defined as [4]

$$\frac{\partial}{\partial \mathbf{n}} = \cos\alpha_\mathrm{n} \sin\beta_\mathrm{n} \frac{\partial}{\partial x} + \sin\alpha_\mathrm{n} \sin\beta_\mathrm{n} \frac{\partial}{\partial y} + \cos\beta_\mathrm{n} \frac{\partial}{\partial z} \,, \tag{7}$$

with α_n being the azimuth of the orientation of $\mathbf{n}$ and β_n being the colatitude. For the present case of $\mathbf{n}$ pointing in positive x-direction, $\partial/\partial\mathbf{n}$ simplifies to $\partial/\partial x$.

Recall that we assume stationary conditions and time-harmonic signals in this paper. We may express $S(\mathbf{x}, \omega)$ as

$$S(\mathbf{x}, \omega) = A(\mathbf{x}, \omega) e^{\mathrm{i}\phi(\mathbf{x}, \omega)} \tag{8}$$

with purely real amplitude $A(\mathbf{x}, \omega) = |S(\mathbf{x}, \omega)|$ and purely real phase $\phi(\mathbf{x}, \omega) = \angle S(\mathbf{x}, \omega)$. Dif-

ferentiation of (8) with respect to any of the Cartesian dimensions yields

$$\begin{aligned}\left(A(\mathbf{x},\omega)e^{\mathrm{i}\phi(\mathbf{x},\omega)}\right)' &= A'(\mathbf{x},\omega)e^{\mathrm{i}\phi(\mathbf{x},\omega)} + A(\mathbf{x},\omega)\left(e^{\mathrm{i}\phi(\mathbf{x},\omega)}\right)' \\ &= \left[A'(\mathbf{x},\omega) + A(\mathbf{x},\omega)\mathrm{i}\phi'(\mathbf{x},\omega)\right]e^{\mathrm{i}\phi(\mathbf{x},\omega)} \\ &\backsimeq A(\mathbf{x},\omega)\phi'(\mathbf{x},\omega)e^{\mathrm{i}\phi(\mathbf{x},\omega)+\mathrm{i}\frac{\pi}{2}}\,, \end{aligned} \tag{9}$$

where in the last step we made use of the stipulated assumption that the high-frequency limit applies, i.e. $\left|\frac{\partial}{\partial\mathbf{n}}A(\mathbf{x},\omega)\right| \ll \left|\frac{\omega}{c}\mathbf{n}A(\mathbf{x},\omega)\right|$, which is known as the *eikonal approximation* [6].

Recall that (2) states that $D(\mathbf{x}_0,\omega) \propto \left(A(\mathbf{x},\omega)e^{\mathrm{i}\phi(\mathbf{x},\omega)}\right)'\big|_{\mathbf{x}=\mathbf{x}_0}$. We can deduce from (9) that, in the high-frequency limit, the phase profile $\phi(\mathbf{x}_0,\omega)$ of the driving function $D(\mathbf{x}_0,\omega)$ is identical to the phase profile of the desired sound field on the secondary source contour and the term $A(\mathbf{x},\omega)\phi'(\mathbf{x},\omega)$ in (9) represents the (purely real) weight profile to be applied.

References

[1] J. Ahrens. *Analytic Methods of Sound Field Synthesis*. Springer-Verlag, Berlin, Heidelberg, 2012.

[2] J. Ahrens. "A linear sensor array with self-bending sensitivity." In *IEEE International Conference on Acoustics, Speech and Signal Processing (ICASSP)*. Shanghai, China, 2016.

[3] J. Ahrens. "Amplitude engineering for beamformers with self-bending directivity based on convex optimization." In *IEEE Workshop on Applications of Signal Processing to Audio and Acoustics*, pages 116–120. New Paltz, NY, 2017.

[4] G. B. Arfken and H. J. Weber. *Mathematical Methods for Physicists*. Elsevier Academic Press, Burlington, MA, sixth edition, 2005.

[5] M. V. Berry and N. L. Balazs. "Nonspreading wave packets." *A. J. Phys.*, 47(3), 264–267, 1979.

[6] M. Born and E. Wolf. *Principles of Optics*. Pergamon Press, Oxford, UK, fourth edition, 1970.

[7] S. Boyd. "Convex optimization examples." Lecture notes (EE364), Stanford University, 2017.

[8] E. Fisher and B. Rafaely. "Near-field spherical microphone array processing with radial filtering." *IEEE TASL*, 19(2), 256–265, 2011.

[9] E. Greenfield, M. Segev, W. Walasik, and O. Raz. "Accelerating light beams along arbitrary convex trajectories." *Phys. Rev. Lett.*, 106(213902), 2011.

[10] W. Herbordt. *Sound capture for human/machine interfaces*. Springer-Verlag, Berlin, Heidelberg, 2005.

[11] R. Kennedy, T. Abhayapala, and D. Ward. "Broadband nearfield beamforming using a radial beampattern transformation." *IEEE Transactions on Signal Processing*, 46(8), 2147–2156, 1998.

[12] H. Lebret and S. Boyd. "Antenna array pattern synthesis via convex optimization." *IEEE Transactions on Signal Processing*, 45(3), 526–532, 1997.

[13] E. Mabande, A. Schad, and W. Kellermann. "Design of robust superdirective beamformers as a convex optimization problem." In *IEEE International Conference on Acoustics, Speech, and Signal Processing (ICASSP)*. 2009.

[14] G. A. Siviloglou and D. N. Christodoulides. "Accelerating finite energy Airy beams." *Optics Letters*, 32(8), 2007.

[15] H. L. van Trees. *Optimum Array Processing*. Wiley, New York, 2002.

[16] E. Williams. *Fourier Acoustics: Sound Radiation and Nearfield Acoustical Holography*. Academic Press, London, UK, 1999.

[17] P. Zhang, T. Li, J. Zhu, X. Zhu, S. Yang, Y. Wang, X. Yin, and X. Zhang. "Generation of acoustic self-bending and bottle beams by phase engineering." *Nature Communications*, 5(4316), 1–9, 2014.

[18] S. Zhao, Y. Hu, J. Lu, X. Qiu, J. Cheng, and I. Burnett. "Delivering sound energy along an arbitrary convex trajectory." *Scientific Reports*, 4(6628), 1–6, 2014.

[19] J. R. Zheng, R. A. Goubran, and M. El-Tanany. "Robust near-field adaptive beamforming with distance discrimination." *IEEE Transactions on Speech and Audio Processing*, 12(5), 478–488, 2004.